Compressed sensing MRI using data-driven tight frame and total generalized variation

Jianping Huang, Lihui Wang, Chunyu Chu, Wanyu Liu, Isabelle Magnin, Yuemin Zhu

Compressed sensing MRI using data-driven tight frame and total generalized variation

Jianping Huang[1,2,3], Lihui Wang[4], Chunyu Chu[2], Wanyu Liu[2,3], Isabelle E. Magnin[2,3] and Yuemin Zhu[2,3]

[1] College of Mechanical and Electrical Engineering, Northeast Forestry University, Harbin 150040, Heilongjiang Province, China
[2] Metislab, CNRS-Inserm, University of Lyon, Harbin Institute of Technology, Harbin, Heilongjiang, 150001, China
[3] CREATIS, CNRS UMR5220, Inserm U1206, INSA Lyon, University of Lyon, Lyon, France
[4] College of computer science and technology, Guizhou University, Huaxi District, 550025, Guiyang, China

Abstract

Undersampling k-space data is an efficient way to reduce the acquisition time of magnetic resonance imaging (MRI). This paper proposes a compressed sensing (CS) method for reconstructing magnetic resonance (MR) images from highly undersampled k-space data. The method is based on the combined use of data-driven tight frame (TF) and total generalized variation (TGV) regularization. The data-driven TF is used to adaptively learn a set of filters from the under-sampled data to provide a better sparse approximation of images. The TGV allows selectively regularizing different image regions to avoid staircase effect. The proposed reconstruction problem is solved by Fast Composite Splitting Algorithm (FCSA). The results on various MR images demonstrated that, for a large range of sampling ratios from 10% to 50%, the proposed method improves reconstruction quality and preserves different image features including edges and textures in comparison with other commonly used CS-MRI methods based on predefined transforms such as the discrete wavelet transform, framelets and shearlet.

Keywords MR image reconstruction, compressed sensing (CS), data-driven tight frame (TF),·total generalized variation (TGV), Fast Composite Splitting Algorithm (FCSA)

1. Introduction

Magnetic resonance imaging (MRI) is a non-invasive medical imaging technique widely used to investigate the anatomy and function of the body in clinical diagnosis. However, the imaging speed of MRI is often limited because of the important quantity of k-space data to acquire. Reducing the acquisition time of MRI therefore remains a great challenge for clinical applications. Numerous efforts have been dedicated to designing fast acquisition sequences and reducing the amount of data required as much as possible while maintaining reconstruction quality [1–8]. Among them, parallel imaging (PI) emerged as the most widely used technique in clinical routine. There are a variety of PI methods such as simultaneous acquisition of spatial harmonics (SMASH) [9], sensitivity encoding (SENSE) [10], generalized autocalibrating partially parallel acquisitions (GRAPPA) [11], and iterative self-consistent parallel imaging reconstruction (SPIRiT) [12]. However, the PI techniques are typically limited by Nyquist sampling rate and the achieved acceleration is limited to low factor values [8].

Recently, the emergence of compressed sensing (CS) [13,14] methods provides a new approach to reconstructing magnetic resonance (MR) images with high quality from significantly under-sampled k-space data, called the CS-MRI, which assumes that MR images have a sparse representation in certain domain (image or transform domain) [15,16]. CS-MRI exploits the sparsity of signals or images to reconstruct the MR images from far fewer samples than conventional methods, and consequently, it allows reducing MRI scanning time efficiently without degrading image quality [8,17,18].

Sparsity or compressibility is a fundamental premise underlying CS-MRI. The first CS-MRI reconstruction method was proposed in [17], which achieved reconstruction by combining total variation (TV) and wavelets as sparsifying transforms. However, since the TV model favours piecewise constant image structures, such TV model-based methods blur details and cause blocking effect with fine structures lost, although the edges are preserved in reconstruction. To overcome the intrinsic drawback of the TV model, various extensions of this model have been proposed for CS-MRI image reconstruction, such as nonlocal total variation (NLTV)

[19,20] and total generalized variation (TGV) [21–23]. These methods can avoid the staircase artifacts that are common to TV and wavelet regularizations, while better preserving image edges and details.

Another common sparsity used for CS-MRI reconstruction is based on the discrete wavelet transform (DWT) [24–28]. It is well known that traditional wavelets transform appropriately point-like singularities, but generally lack performance when dealing with singularities in higher dimension, such as edges, contours or regular textures in two-dimensional (2D) images [29]. To overcome the limitation, multi-scale geometric analysis method is introduced into CS-MRI in order to more sparsely represent piecewise smooth images containing rich geometric information (e.g. edges, curves, etc.), such as contourlets [30,31], framelets [32], and shearlets [23,33].

Data adaptive transforms can sparsify images better than those explored in various image-processing problems in recent years. Instead of predefined transforms, Hong et al [34] proposed a data-adaptive sparsifying transform using singular value decomposition (SVD) for CS-MRI image reconstruction. This method can be applied to a broader range of MR images to improve image reconstruction quality effectively. In [35], an adaptive data-driven tight frame (data-driven TF) was proposed to solve image restoration problems, and has been successfully applied to image denoising and seismic data restoration problems . Dictionary learning approaches learn a dictionary as a sparse basis from the elemental patches of particular image instance or class of images to achieve better sparsity of the input image in CS-MRI [36,37]. However, these methods ignored the relationship between image patches in dictionary learning and sparse coding. Meanwhile, an adaptive nonlocal processing was also introduced for image restoration [38–40]. By combining the notion of patches and nonlocal processing, a patch-based nonlocal operator was introduced for CS-MR image reconstruction [41]. This kind of methods is based on grouping similar 2-D image patches into 3-D data arrays, and then 3-D transforming the data arrays to obtain sparsity. Since the methods exploit the nonlocal self-similarity of images, it becomes possible to achieve lower reconstruction errors and higher visual quality, compared with the conventional CS-MRI reconstruction methods.

In this paper, we propose a CS method for reconstructing MR images from highly undersampled k-space data. The method is based on the combined use of data-driven tight frame (TF) and total generalized variation (TGV) regularization. The data-driven TF is used to adaptively learn a set of filters from the under-sampled data to provide a better sparse approximation of images. The TGV allows selectively regularizing different image regions to avoid staircase effect. The proposed reconstruction problem is solved by Fast Composite Splitting Algorithm (FCSA).

The rest of the paper is organized as follows. The proposed CS-MRI reconstruction method is detailed in Section 2. The experiments and results are presented in Section 3, followed by conclusion in Section 4.

2. Methodology

2.1. Preliminaries

Tight Frame (TF) [42,43] : The *frame* is a generalized concept of the *basis* formed of linearly dependent vectors. Specifically, a set of vectors $\{\varphi_i\}_i^n \subset H$ is a frame in Hilbert space H, if there exist two positive constants A and B, such that for any vector $x \in H$:

$$A\|x\|_2^2 \le \sum_i \left|\langle \varphi_i, x\rangle\right|^2 \le B\|x\|_2^2. \tag{1}$$

when the constants $A = B = 1$, the frame $\{\varphi_i\}_i^n$ is called the *tight frame (TF)*.

For a given frame $\{\varphi_i\}_i^n$, two associated operators can be defined: the analysis operator Ψ defined by

$$\Psi : x \in H \to \left\{\langle x, \varphi_i\rangle\right\} \in l^2(N), \tag{2}$$

and the synthesis operator (adjoint operator of the analysis operator):

$$\Psi^T : \{c_i\} \in l^2(N) \to \sum_i c_i \varphi_i \in H. \tag{3}$$

The sequence $\{\varphi_i\}_i^n$ forms a tight frame if and only if $\Psi^T\Psi = I$ with I designating the identity operator.

A tight frame can be constructed from a set of filters based on the Unitary Extension Principle (UEP) proposed in [44]. Given a set of filters $\{a_i\}_i^n$, the analysis operator Ψ can be defined as

$$\Psi = \left[S_{a_1}^T, S_{a_2}^T, \cdots, S_{a_n}^T \right]^T \tag{4}$$

and its adjoint operator (synthesis operator) Ψ^T by

$$\Psi^T = \left[S_{a_1}, S_{a_2}, \cdots, S_{a_n} \right]. \tag{5}$$

here, S_a refers to the linear convolution operator. For a filter with finite support, the convolution operation can be represented by a block-wise Toeplitz matrix under Neumann boundary conditions [45]. For example, the discrete wavelet tight frame is one of the widely used tight frames, which is generated by a set of filters called framelet filter h_i (corresponding to a_i).

Data-driven TF [35] : A tight frame simply constructed from predefined filters can sparsely represent certain classes of data. However, it is not efficient when the image structure is complex (for example for complex geometric structures, rich textures, etc.). The data-driven TF is then proposed that is constructed from a set of filters adaptively learned from the input data itself to sparsely represent the given data. Given an image x, a set of filters $\{a_i\}_i^n$ (the size of a_i is $\sqrt{n} \times \sqrt{n}$) can be learned by solving the following minimization problem [35]

$$\min_{\nu,\Psi} \|\nu - \Psi x\|_2^2 + \gamma \cdot \|\nu\|_0, \quad \text{subject to } \Psi^T \Psi = I, \tag{6}$$

where ν is the coefficient vector that sparsely approximates the tight frame coefficients Ψx, and $\gamma > 0$ a regularization parameter. The detailed and complete description of the data-driven TF construction scheme and numerical solver can be found in [35]. An example of the data-driven TF filters constructed with two different sizes is shown in Fig. 1 (a small image block represents a filter).

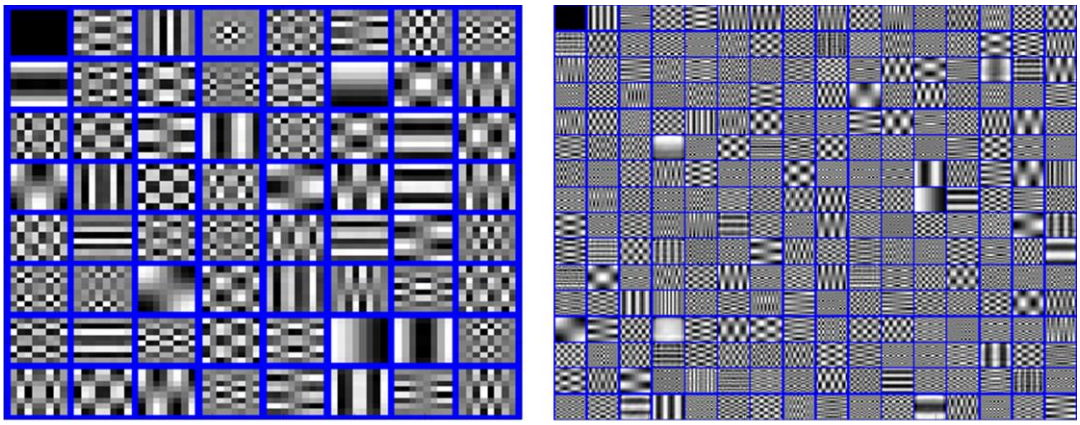

Fig. 1. Illustration the data-driven TF filters constructed with two different sizes. (a) Filter (atom) size 8×8, (b) Filter (atom) size 16×16.

Total generalized variation (TGV) [21,22] : Unlike TV regularization, which preserves sharp edges but blurs some details and causes blocking effect with fine structures lost, the TGV is a direct extension of the classical TV semi-norm and the regularization term is convex. The TGV selectively regularizes different image regions at different levels and thus leads to better performance by preserving edges and suppressing the staircase effect [21,22]. The discrete TGV of second-order formulated by [22] is

$$\mathrm{TGV}_\alpha^2(u) = \min \alpha_1 \int_\Omega |\nabla u - v| dx + \alpha_0 \int_\Omega |\varepsilon(v)| dx \tag{7}$$

where $\varepsilon(v) = \frac{1}{2}\left(\nabla v + \nabla v^T\right)$ denotes the symmetrized derivative, α_0 and α_1 are the positive weights.

2.2. Proposed model

Assuming that x is a MR image and F_u is a partial Fourier transform which can be expressed by $F_u = P \cdot F$, with F the Fourier transform and P the common under-sampling pattern (mask). The under-

sampled measurements b of the image x with an unknown observation noise ε in k-space is then defined as [18]:

$$b = F_u x + \varepsilon . \tag{8}$$

For the under-sampling case, Eq. (8) is highly underdetermined and has therefore an infinity of solutions. In order to find the optimal solution to this problem, additional constraints are introduced into the CS framework according to some prior knowledge. Thus, the CS-MRI reconstruction can be formulated as the following optimization problem

$$x = \arg\min_x \left\| F_u x - b \right\|_2^2 + \lambda \cdot J(x), \tag{9}$$

where $J(x)$ is a regularizing functional and $\lambda > 0$ denotes a balancing parameter.

Now, by introducing the above-stated data-driven TF and TGV regularization, we can formulate the CS-MRI reconstruction as the following optimization problem

$$x = \arg\min_x \left\{ \frac{1}{2} \left\| F_u x - b \right\|_2^2 + \lambda \cdot \left\| \Psi x \right\|_1 + \beta \cdot \mathrm{TGV}_\alpha^2(x) \right\}. \tag{10}$$

In the formula, the first term $\left\| F_u x - b \right\|$ is a data fidelity term, the second term $\left\| \Psi x \right\|_1$ and the third term $\mathrm{TGV}_\alpha^2(x)$ are regularization terms, and λ and β are the regularization parameters. Ψ is the data-driven TF described above, $\mathrm{TGV}_\alpha^2(x)$ refers to the second-order TGV of the image x, where, according to [22], the weights α_0 and α_1 appearing in Eq. (7) do not need to be tuned and are set to 2 and 1, respectively.

The proposed optimization problem (Eq. (10)) can be solved by the Fast Composite Splitting Algorithm (FCSA) proposed in [46]. Let $f(x) = \frac{1}{2} \left\| F_u x - b \right\|_2^2$, which is a convex and smooth function with Lipschitz constant L, and $g(x) = \lambda \cdot \left\| \Psi x \right\|_1 + \beta \cdot \mathrm{TGV}_\alpha^2(x)$ denoted as a regularizing functional. According to the FCSA algorithm framework, the $g(x)$ problem can be divided into two sub-problems: the regularization of l_1-norm and TGV. Thus, $g(x)$ can be expressed as $g(x) = g_1(x) + g_2(x)$, where $g_1(x) = \lambda \cdot \left\| \Psi x \right\|_1$ and $g_2(x) = \beta \cdot \mathrm{TGV}_\alpha^2(x)$. Each sub-problem is actually a convex function which can be solved by a proximal mapping operation. Given a continuous convex function $\varphi(x)$, the proximal map is described as [46]:

$$prox_\rho(\phi)(x) = \arg\min \left\{ \phi(u) + \frac{1}{2\rho} \left\| u - x \right\|_2^2 \right\}, \tag{11}$$

where scalar $\rho > 0$ is the inverse of the Lipschitz constant L of ∇f defined [46] by $\nabla f = \frac{\partial}{\partial x} \left(\frac{1}{2} \left\| F_u x - b \right\|_2^2 \right) = F_u^T \left(F_u x - b \right)$, with F_u^T denotes the inverse partial Fourier transform.

Then, the regularization of l_1-norm sub-problem is achieved via solving the following minimization

$$prox_\rho(g_1)(x) = \arg\min_u \left\{ \frac{1}{2\rho} \left\| u - x \right\|_2^2 + \lambda \cdot \left\| \Psi^k u \right\|_1 \right\}. \tag{12}$$

Eq. (12) is solved using an iterative thresholding algorithm under a tight frame [35].

The TGV regularization sub-problem is formulated as

$$prox_\rho(g_2)(x) = \arg\min_u \left\{ \frac{1}{2\rho} \left\| u - x \right\|_2^2 + \beta \cdot TGV_\alpha^2(u) \right\}. \tag{13}$$

Eq. (13) can be solved using the first-order primal-dual algorithm. More details about this algorithm can be found in [22].

The proposed algorithm is outlined in Table 1.

Table 1

Outline of the proposed CS-MRI reconstruction algorithm

INPUT:

K : the maximum number of iterations;

n : the filter size of data-driven TF;

λ, β : the regularization parameters;

η : the tolerance parameter;

INIT:

Set $\rho = 1/L, t^1 = 1, x^0 = r^1 = 0, k = 0;$

OUTPUT:

x : reconstructed image.

REPEAT:

$k = k + 1;$

Generate the analysis operator Ψ^k according to Eq. (6);

$$x_g = r^k - \rho \nabla f\left(r^k\right);$$

$$x_1 = prox_\rho\left(2\lambda \left\|\Psi^k x\right\|_1\right)\left(x_g\right);$$

$$x_2 = prox_\rho\left(2\beta \cdot TGV_\alpha^2(x)\right)\left(x_g\right);$$

$$x^k = \frac{x_1 + x_2}{2};$$

$$t^{k+1} = \frac{1+\sqrt{1+4\left(t^k\right)^2}}{2};$$

$$r^{k+1} = x^k + \frac{t^k - 1}{t^{k+1}}\left(x^k - x^{k-1}\right);$$

UNTIL $k > K$ **OR** $\dfrac{\left\|x^{k-1} - x^k\right\|_2}{\left\|x^k\right\|_2} < \eta$

3. Experiments results and Discussion

3.1. Experimental setup

To evaluate the performance of the proposed method, the MR images of size 256×256 from [20,24,46] were used, as shown in Fig. 2(b)-(e). In Fig. 2(a) is shown the k-space sampling mask where the k-space data is sampled with a rate of 15% (i.e. keeping 15% of the complete k-space data) using variable density undersampling pattern [17]. The proposed method was also compared with existing state of the art CS-MRI methods based on the commonly used sparsifying transforms, including the SparseMRI [17], FCSA [46], Framelet+NLTV [32], Shearlet+TGV [23]. For fair comparisons, all codes were downloaded from the authors' website and the corresponding experimental setup was carefully followed.

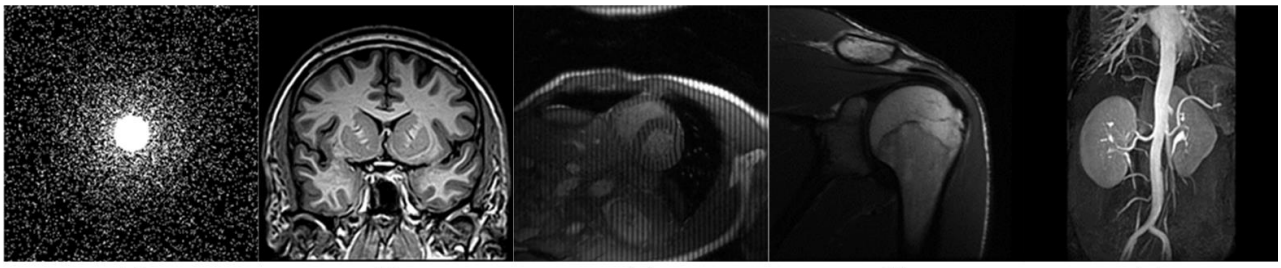

(a) (b) (c) (d) (e)

Fig. 2. k-space undersampling mask and MR images. (a) k-space sampling mask, (b) Coronal brain, (c) Cardiac, (d) Shoulder, (e) Renal arteries.

The observation measurement b was modeled as $b = F_u x + \varepsilon$, where ε represents complex Gaussian white noise with standard deviation σ_n. The associated input SNR (ISNR) [47] is defined as $\mathrm{ISNR} = 20\log_{10}\left(\frac{\sigma_x}{\sigma_n}\right)$, with σ_x denoting the standard deviation of the original image. In the proposed method, the filter size of data-driven TF was set as 8×8, the regularization parameter λ in the soft-thresholding operator as $0.1\times\sigma_n$, the regularization parameter β as 0.05, and the ISNR as 30 dB. Note that, in the proposed method, since the filter size of data-driven TF has non negligible influence on computation time, to assess the influence of filter size on reconstruction results, several filter sizes were tested, including 2×2, 4×4, 8×8, 10×10, 16×16.

In addition to the visual assessment, three quantitative indices were calculated for the MR images reconstructed with different methods. They are the peak-signal-to-noise ratio (PSNR), relative *l2* norm error (RLNE) [28] and mean structural similarity (MSSIM) [48]. PSNR and RLNE are used for measuring reconstruction accuracy, and MSSIM is used for evaluating the structural similarity between reconstructed and reference images.

The PSNR is defined as

$$\mathrm{PSNR} = 20\log_{10}\left(\frac{MAX_x}{\sqrt{MSE}}\right), \tag{14}$$

where $\mathrm{MSE} = \frac{1}{M\times N}\sum_{i=1}^{M}\sum_{j=1}^{N}\left[x(i,j)-x(i,j)\right]^2$ and MAX_x is the maximum possible pixel value of the image, which is set to be 1 or 255.

The RLNE is given by

$$\mathrm{RLNE} = \frac{\left\|x_{ref} - x_{rec}\right\|_2}{\left\|x_{ref}\right\|_2} \tag{15}$$

where x_{ref} and x_{rec} denote the images reconstructed from respectively full and partial k-spaces.

The SSIM is defined as

$$\mathrm{SSIM}(x,y) = \frac{\left(2\mu_x\mu_y + C_1\right)\left(2\sigma_{xy} + C_2\right)}{\left(\mu_x^2 + \mu_y^2 + C_1\right)\left(\sigma_x^2 + \sigma_y^2 + C_2\right)} \tag{16}$$

where the parameters C_1 and C_2 are constants that avoid instability when the local means μ_x, μ_y and local standard deviations σ_x, σ_y are close to zero. The mean SSIM (MSSIM) is a single value that represents an overall quality measure of the entire image. The MSSIM values exhibit much better consistency with qualitative visual appearance [48].

The experiments were performed on a PC computer with Intel (R) Core (TM) i5-2400 3.1GHz CPU, 4.00GB memory and Windows 7 SP1, MATLAB Version 7 platform.

3.2. Visual comparison

Figs. 3-6 show the visual comparison of the MR images reconstructed using different methods. The sampling ratio was set to be approximately 15%. It is seen that the proposed method provides more satisfying results with clear contours, sharp edges and fine image details.

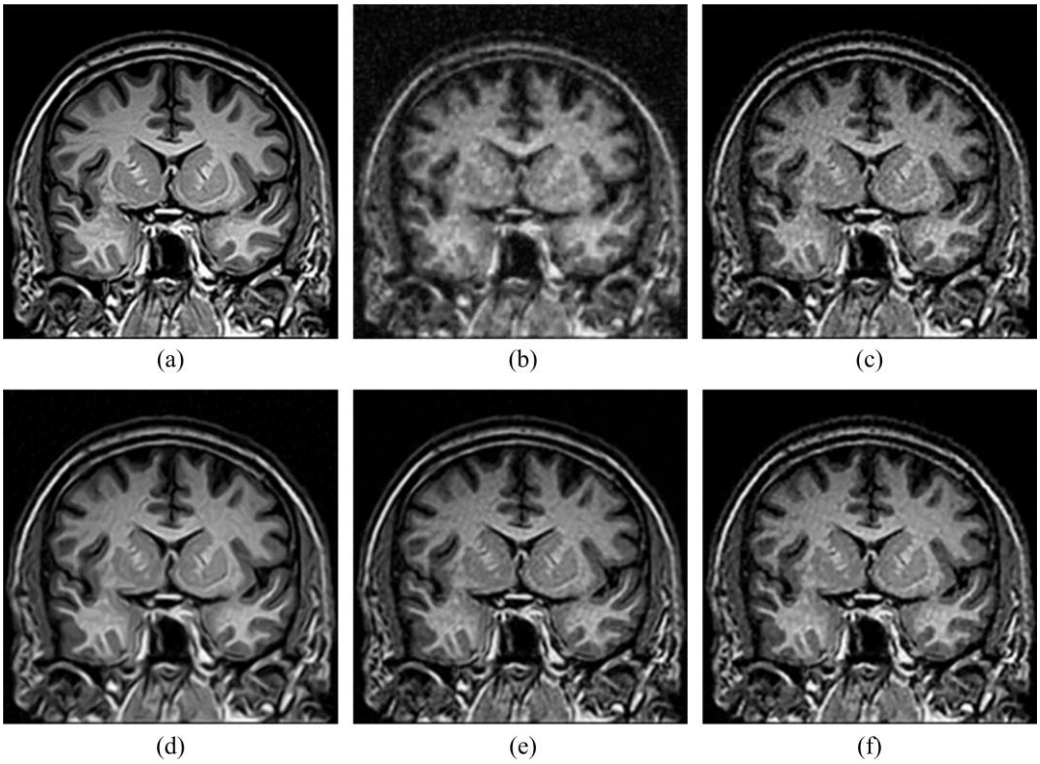

Fig. 3. Results of reconstruction on the coronal brain MR image using different methods with 15% sampling. (a) Original MR images, images reconstructed by, (b) SparseMRI, (c) FCSA, (d) Framelet+NLTV, (e) Shearlet+TGV, (f) Data-driven TF+TGV (proposed).

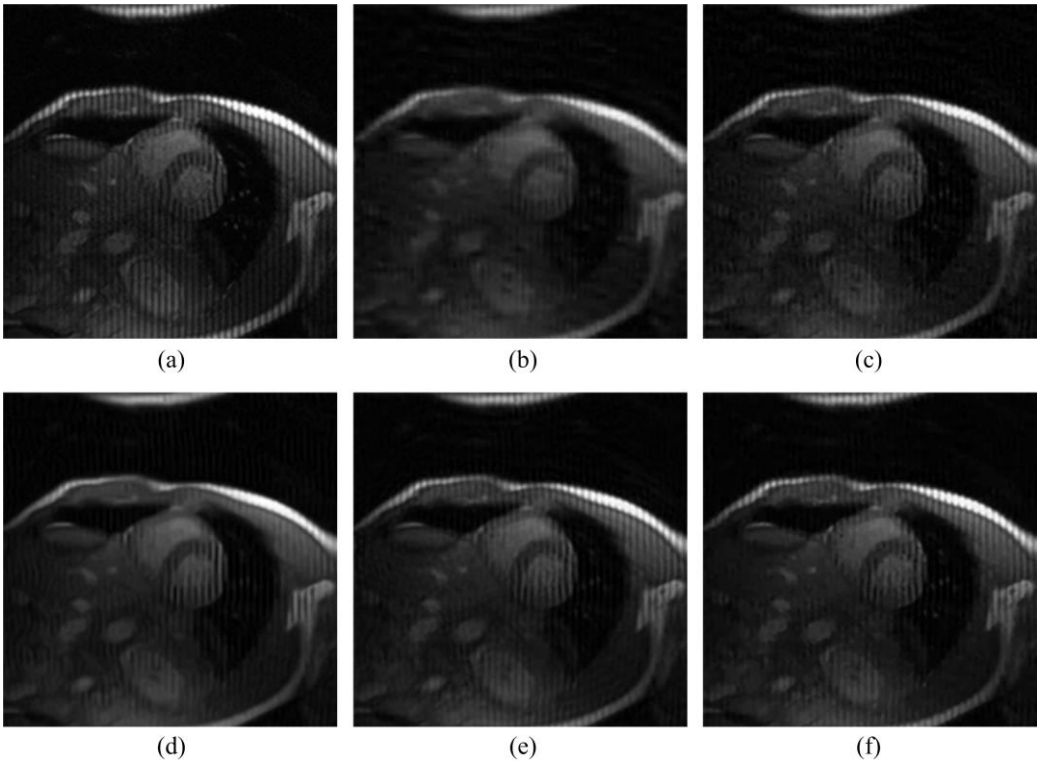

Fig. 4. Results of reconstruction on the cardiac MR image using different methods with 15% sampling. (a) Original MR images; images reconstructed using, (b) SparseMRI, (c) FCSA, (d) Framelet+NLTV, (e) Shearlet+TGV, (f) Data-driven TF+TGV (proposed).

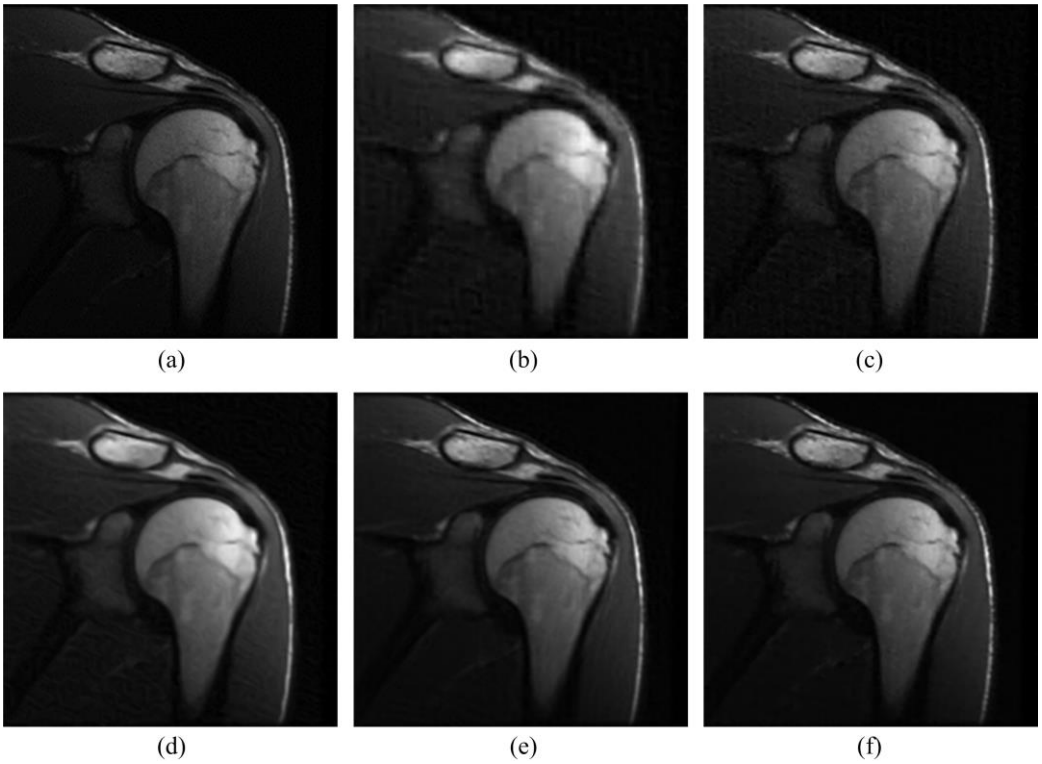

Fig. 5. Results of reconstruction on the shoulder MR image using different methods with 15% sampling. (a) Original MR images; images reconstructed using, (b) SparseMRI, (c) FCSA, (d) Framelet+NLTV, (e) Shearlet+TGV, (f) Data-driven TF+TGV (proposed).

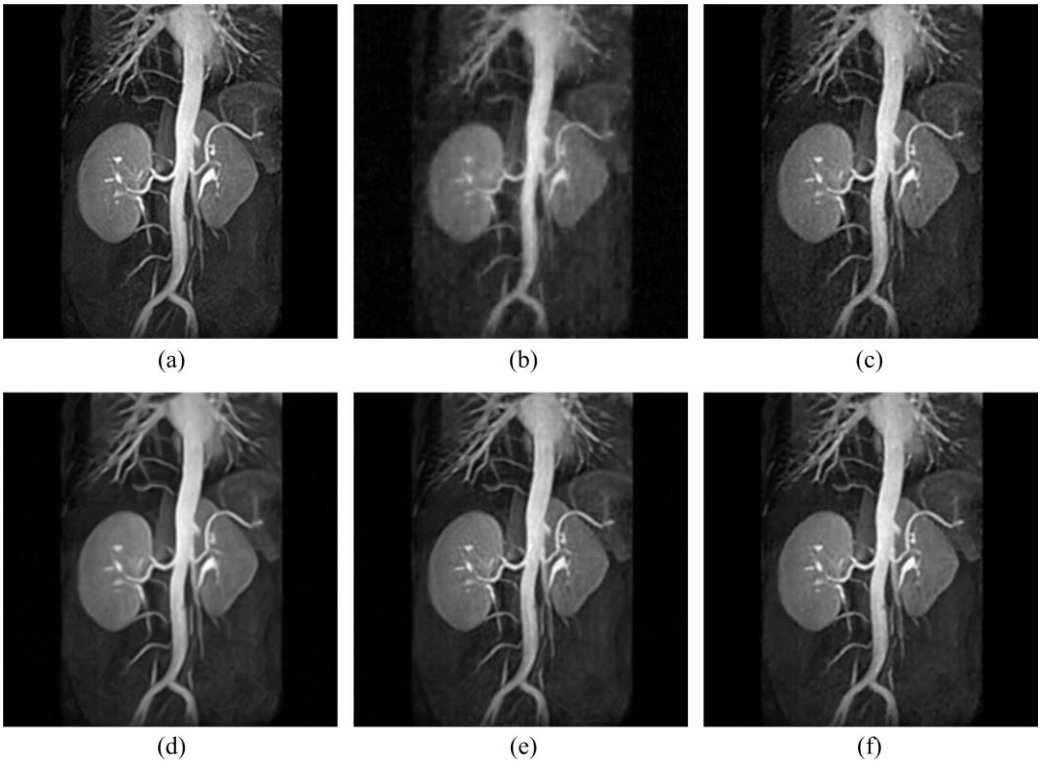

Fig. 6. Results of reconstruction on the renal arteries MR image using different methods with 15% sampling. (a) Original MR images; images reconstructed using, (b) SparseMRI, (c) FCSA, (d) Framelet+NLTV, (e) Shearlet+TGV, (f) Data-driven TF+TGV (proposed).

More quantitatively, the PSNR, RLNE and MSSIM indices calculated for the MR images reconstructed with the different methods are given in Tables 2 to 4. It can be observed that the proposed method improves the reconstruction performance in comparison with existing methods, by providing higher PSNRs, smaller RLNEs, and greater MSSIMs.

Table 2
PSNR of reconstruction on MR images using different methods with 15% sampling

	SparseMRI	FCSA	Framelet+NLTV	Shearlet+TGV	Proposed
Coronal Brain	20.79	26.07	26.25	27.21	**27.59**
Cardiac	30.08	32.44	31.25	33.60	**34.30**
Shoulder	23.86	31.94	25.05	35.08	**38.27**
Renal arteries	26.97	32.21	32.34	33.46	**35.28**

Table 3
RLNE of reconstruction on MR images using different methods with 15% sampling

	SparseMRI	FCSA	Framelet+NLTV	Shearlet+TGV	Proposed
Coronal Brain	0.26	0.14	0.14	0.13	**0.12**
Cardiac	0.19	0.15	0.17	0.13	**0.12**
Shoulder	0.37	0.15	0.32	0.10	**0.07**
Renal arteries	0.16	0.09	0.09	0.08	**0.06**

Table 4
MSSIM of reconstruction on MR images using different methods with 15% sampling

	SparseMRI	FCSA	Framelet+NLTV	Shearlet+TGV	Proposed
Coronal Brain	0.53	0.84	0.85	0.87	**0.88**
Cardiac	0.75	0.80	0.79	0.84	**0.86**
Shoulder	0.82	0.89	0.89	0.96	**0.97**
Renal arteries	0.58	0.88	0.88	0.89	**0.93**

3.3. Effect of sampling rates

In order to investigate the effect of sampling rates on MR image reconstruction, experiments were performed with sampling rates varying from 10% to 50% (corresponding to 0.1~0.5 on the x-axis in the Figs.). The curves of PSNR, RLNE and MSSIM versus different sampling rates for all the MR images reconstructed with different methods are shown in Figs. 7-9. It can be seen that the proposed method almost always outperforms SparseMRI, FCSA, Framelet+NLTV and Shearlet+TGV for different MR image and different sampling rates. For example, as illustrated in Fig. 7(a), Fig. 8(a) and Fig. 9(a) on the coronal brain MR image, the proposed method delivers higher PSNR and MSSIM and lower RLNE than the other methods. These results also imply that, for the same image reconstruction quality, the proposed method requires even fewer samples and as a result allows further shortening acquisition time.

3.4. Effects of filter size

The influence of filter size on reconstruction results are illustrated in Figs. 10-12. We observe that the reconstruction performance (PSNR, RLNE and MSSIM) of the proposed method on different images changed little when the filters size was larger than 2×2. This means that the proposed method is little sensitive to the filter size.

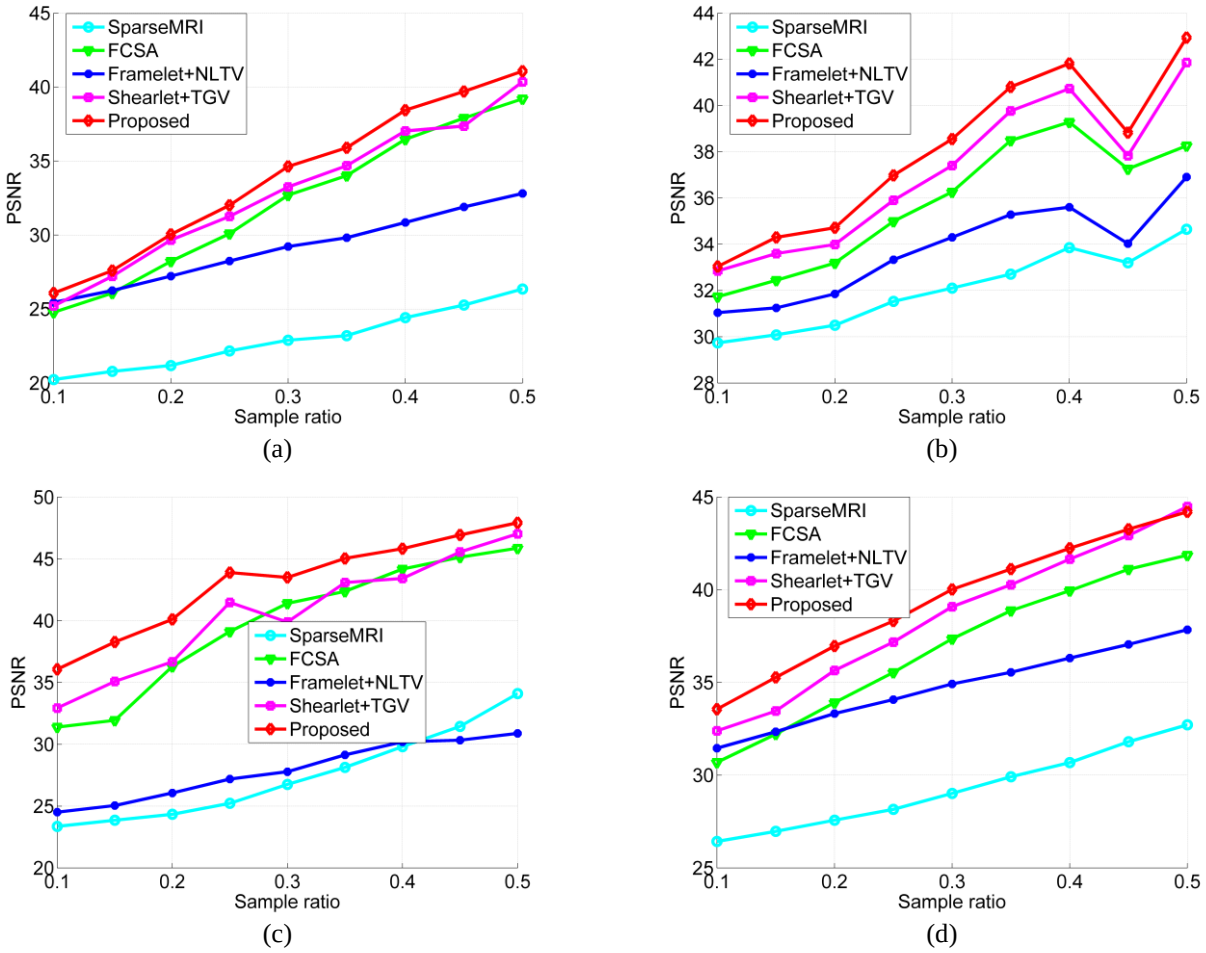

Fig. 7. Comparison of PSNR as a function of sampling rate on different MR images. (a) Coronal brain image, (b) Cardiac image, (c) Shoulder image, (d) Renal arteries image.

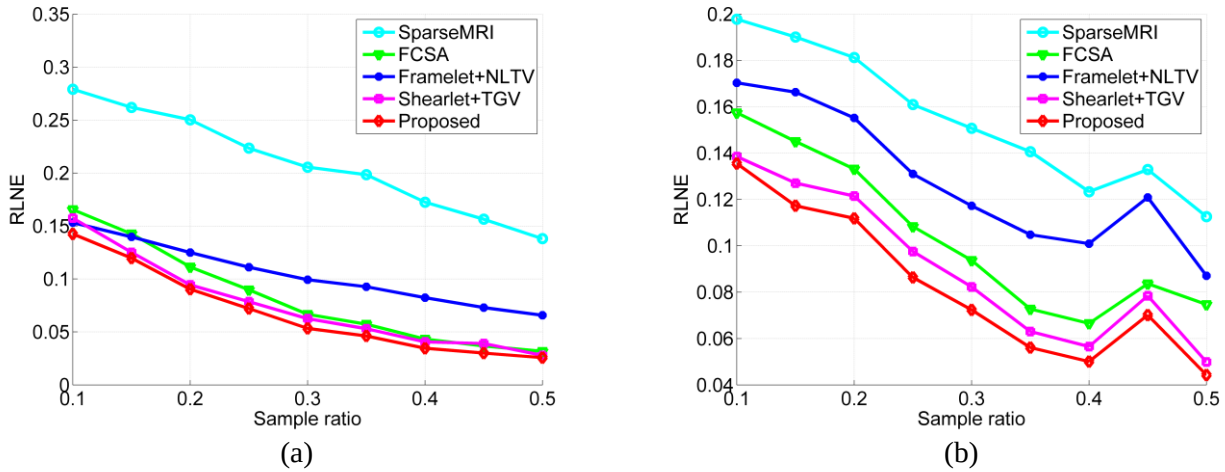

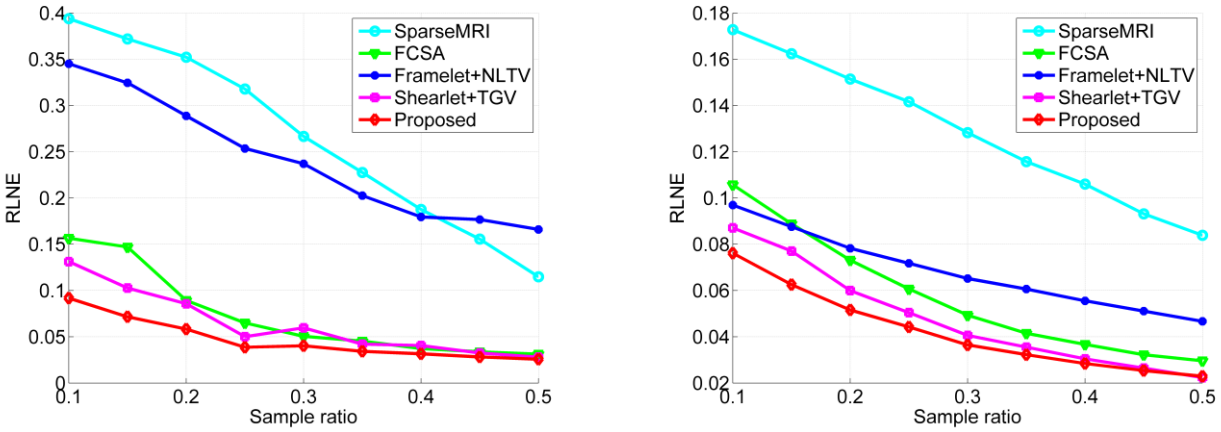

(c) (d)

Fig. 8. Comparison of RLNE as a function of sampling rate on different MR images. (a) Coronal brain image, (b) Cardiac image, (c) Shoulder image, (d) Renal arteries image.

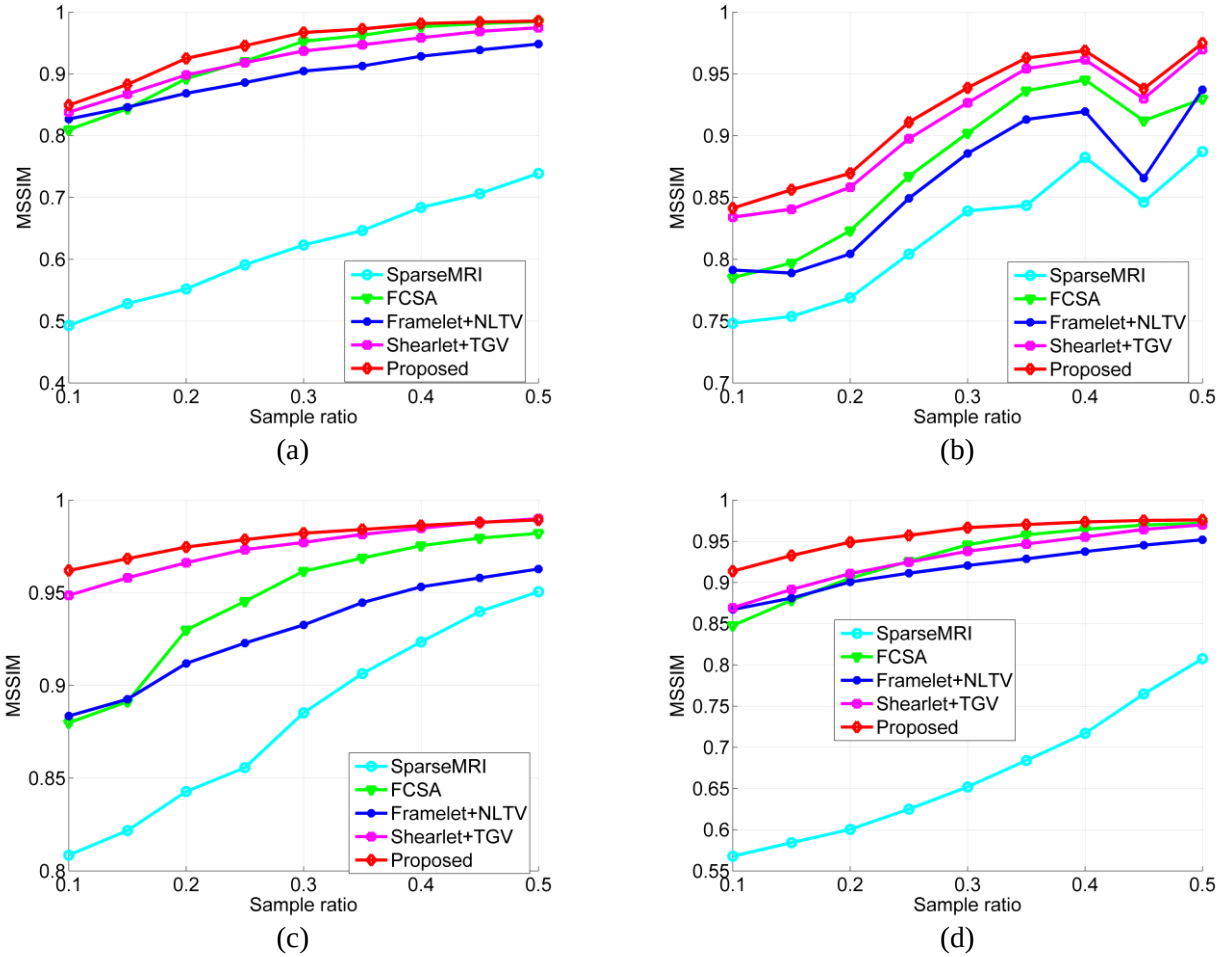

(a) (b)

(c) (d)

Fig. 9. Comparison of MSSIM as a function of sampling rate on different MR images. (a) Coronal brain image, (b) Cardiac image, (c) Shoulder image, (d) Renal arteries image.

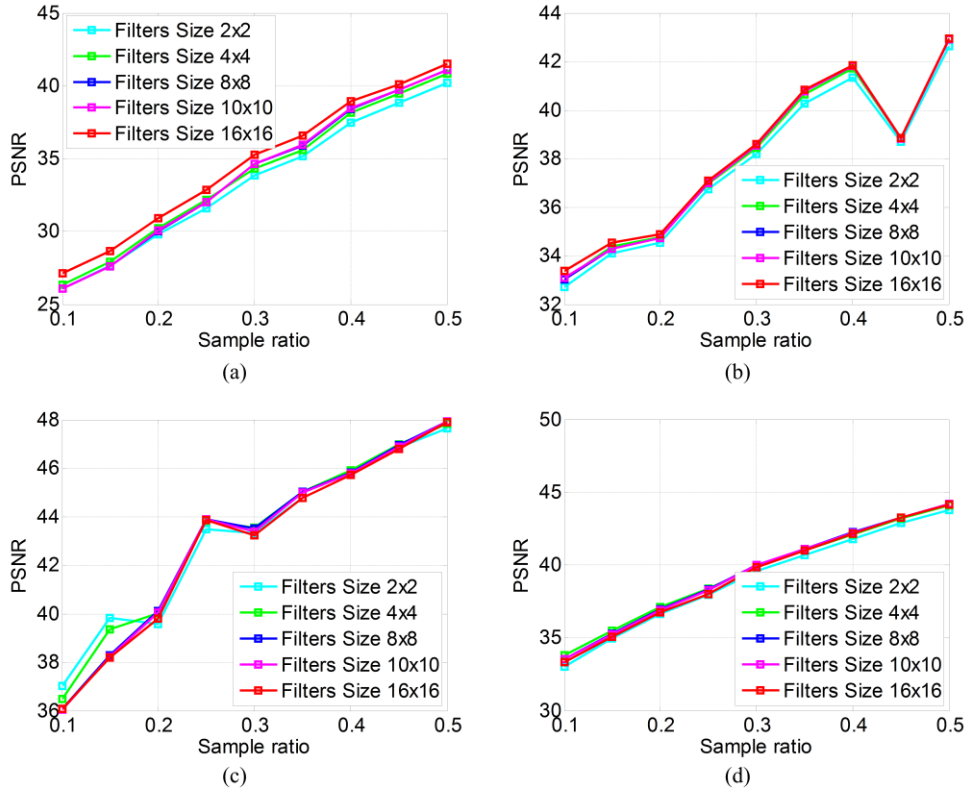

Fig. 10. Comparison of PSNR curves with different filters size. (a) Coronal brain image, (b) Cardiac image, (c) Shoulder image, (d) Renal arteries image.

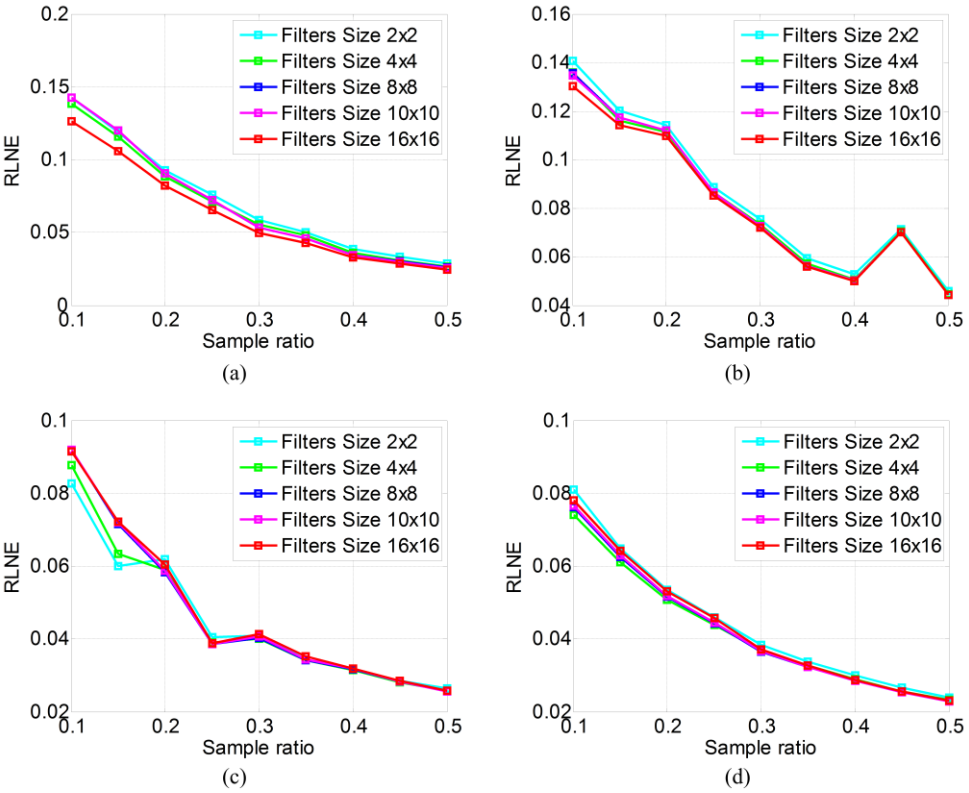

Fig. 11. Comparison of RLNE curves with different filters size. (a) Coronal brain image, (b) Cardiac image, (c) Shoulder image, (d) Renal arteries image.

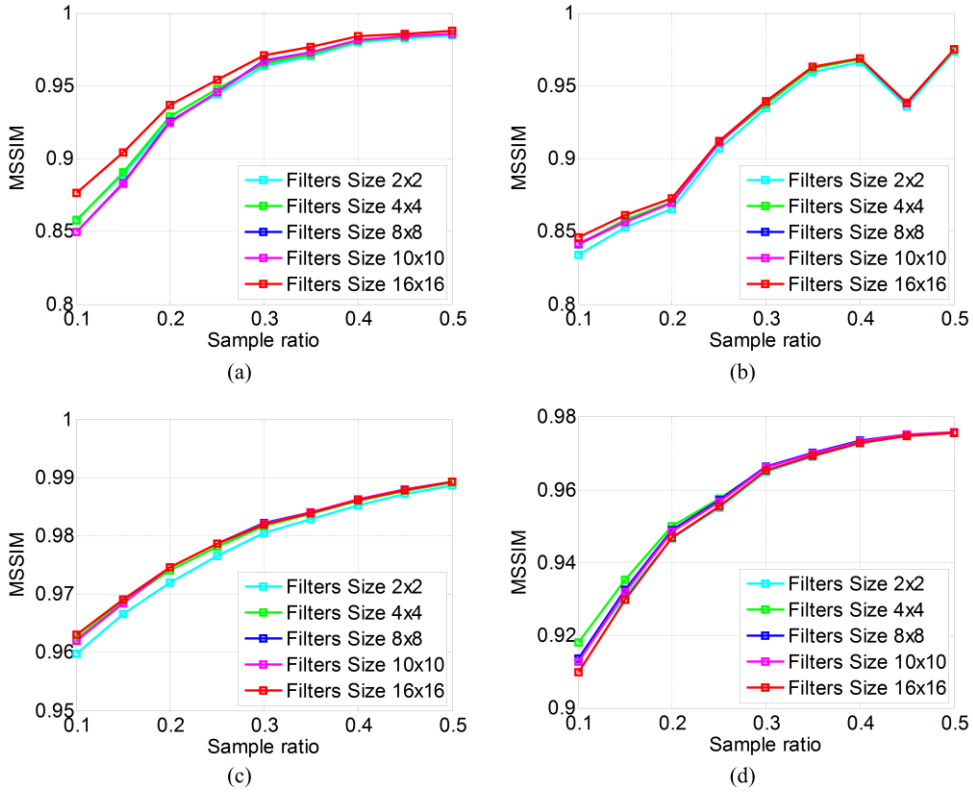

Fig. 12. Comparison of MSSIM curves with different filters size. (a) Coronal brain image. (b) Cardiac image, (c) Shoulder image, (d) Renal arteries image.

3.5. Computation time

Concerning computation time, the comparison between the proposed method and the other methods is given in Table 5 with a sampling ratio of 10%. It can be clearly seen that the FCSA method is the fastest among the four methods, and the proposed method takes the longest time. Moreover, the computation time of the proposed method increases with the increase of the filter size.

Table 5
Comparison of computation time (in second) of different methods on different images with a sampling ratio of 10%

methods \ image	Coronal brain	Cardiac	Shoulder	Renal arteries
FCSA	6.2	5.9	5.9	5.2
SparseMRI	16.7	20.1	19.9	18.1
Shearlet+TGV	87.2	88.6	100.3	58.9
Framelet+NLTV	291.0	288.7	291.8	292.3
Proposed (filters size 2×2)	491.2	491.3	491.4	490.1
Proposed (filters size 4×4)	1559.9	1565.5	1564.2	1567.8
Proposed (filters size 8×8)	6158.6	6172.6	6157.3	6153.0
Proposed (filters size 10×10)	9638.6	9662.9	9653.6	9639.6

4. Discussion and Conclusion

Reducing acquisition time and keeping image quality of MRI remains a great challenge for clinical applications. Many attempts have been made to shorten the acquisition time, such as parallel imaging, partial

k-space imaging and simultaneous multi-slice (SMS) imaging. Compressed sensing MRI is an acceleration technique based on sparse data sampling and iterative reconstruction that allowing scan time reduction while maintaining acceptable image quality.

We have proposed a CS method for reconstructing various types of MR images from highly undersampled k-space data. The method presents the particularity of combining the data-driven TF and TGV to form a new regularization approach, which has enabled us to adaptively generate a set of filters from the undersampled data, obtain a better sparse approximation of MR images, and avoid staircase effects commonly present in TV regularization. The experimental results demonstrated that the proposed method presents better performance than existing state of the art CS-MRI methods for various MR images by preserving edges, suppressing under-sampling artifacts, delivering higher PSNR and MSSIM and lower RLNE at a wide range of sampling rates from 10% to 50%. The improved CS MR image reconstruction method proposed in this work has been shown to produce better reconstruction results for a broad range of MR images, which suggests its potential clinical utility.". In the future work, it would be interesting to work on how to accelerate the computation time of the proposed method.

Acknowledgments

This work was supported in part by the National Natural Science Foundation of China (no. 61701105, 61661010, 61271092), The Natural Science Foundation of Heilongjiang Province project(no. QC2017066), the applied technology research and development program of Heilongjiang Province (no. GC13A311), and the French ANR under MOSIFAH ANR-13-MONU-0009-01.

Conflict of Interest: The authors declare that they have no conflict of interest.

References

[1] McGibney G, Smith MR, Nichols ST, Crawley A. Quantitative evaluation of several partial Fourier reconstruction algorithms used in MRI. Magn Reson Med 1993;30:51–9. doi:10.1002/mrm.1910300109.

[2] Blaimer M, Breuer F, Mueller M, Heidemann RM, Griswold MA, Jakob PM. SMASH, SENSE, PILS, GRAPPA: how to choose the optimal method. Top Magn Reson Imaging 2004;15:223–36. doi:10.1097/01.rmr.0000136558.09801.dd.

[3] Tsao J, Kozerke S. MRI temporal acceleration techniques. J Magn Reson Imaging 2012;36:543–60. doi:10.1002/jmri.23640.

[4] Luo J, Zhu Y, Li W, Croisille P, Magnin IE. MRI reconstruction from 2D truncated k-space. J Magn Reson Imaging 2012;35:1196–206. doi:10.1002/jmri.23538.

[5] Larkman DJ, Nunes RG. Parallel magnetic resonance imaging. Phys Med Biol 2007;52:R15–55. doi:10.1088/0031-9155/52/7/r01.

[6] Xie G, Song Y, Shi C, Feng X, Zheng H, Weng D, et al. Accelerated magnetic resonance imaging using the sparsity of multi-channel coil images. Magn Reson Imaging 2014;32:175–83. doi:10.1016/j.mri.2013.10.010.

[7] Majumdar A, Ward RK. Calibration-Less Multi-coil MR image reconstruction. Magn Reson Imaging 2012;30:1032–45. doi:10.1016/j.mri.2012.02.025.

[8] Hollingsworth KG. Reducing acquisition time in clinical MRI by data undersampling and compressed sensing reconstruction. Phys Med Biol 2015;60:R297–322. doi:10.1088/0031-9155/60/21/r297.

[9] Sodickson DK, Manning WJ. Simultaneous acquisition of spatial harmonics (SMASH): Fast imaging with radiofrequency coil arrays. Magn Reson Med 1997;38:591–603. doi:10.1002/mrm.1910380414.

[10] Pruessmann KP, Weiger M, Scheidegger MB, Boesiger P. SENSE: Sensitivity encoding for fast MRI. Magn Reson Med 1999;42:952–62. doi:10.1002/(SICI)1522-2594(199911)42:5<952::AID-MRM16>3.0.CO;2-S.

[11] Griswold MA, Jakob PM, Heidemann RM, Nittka M, Jellus V, Wang JM, et al. Generalized Autocalibrating Partially Parallel Acquisitions (GRAPPA). Magn Reson Med 2002;47:1202–10. doi:10.1002/mrm.10171.

[12] Lustig M, Pauly JM. SPIRiT: Iterative Self-consistent Parallel Imaging Reconstruction From Arbitrary k-Space. Magn Reson Med 2010;64:457–71. doi:10.1002/mrm.22428.
[13] Candes EJ, Romberg J, Tao T. Robust uncertainty principles: Exact signal reconstruction from highly incomplete frequency information. Ieee Trans Inf Theory 2006;52:489–509. doi:10.1109/tit.2005.862083.
[14] Donoho DL. Compressed sensing. Ieee Trans Inf Theory 2006;52:1289–306. doi:10.1109/tit.2006.871582.
[15] Miao J, Guo W, Narayan S, Wilson DL. A simple application of compressed sensing to further accelerate partially parallel imaging. Magn Reson Imaging 2013;31:75–85. doi:http://dx.doi.org/10.1016/j.mri.2012.06.028.
[16] Majumdar A, Ward RK. Exploiting rank deficiency and transform domain sparsity for MR image reconstruction. Magn Reson Imaging 2012;30:9–18. doi:10.1016/j.mri.2011.07.021.
[17] Lustig M, Donoho D, Pauly JM. Sparse MRI: The application of compressed sensing for rapid MR imaging. Magn Reson Med 2007;58:1182–95. doi:10.1002/mrm.21391.
[18] Lustig M, Donoho DL, Santos JM, Pauly JM. Compressed sensing MRI. IEEE Signal Process Mag 2008;25:72–82. doi:10.1109/msp.2007.914728.
[19] Liang D, Wang H, Chang Y, Ying L. Sensitivity Encoding Reconstruction With Nonlocal Total Variation Regularization. Magn Reson Med 2011;65:1384–92. doi:10.1002/mrm.22736.
[20] Junzhou H, Fei Y. Compressed magnetic resonance imaging based on wavelet sparsity and nonlocal total variation. 2012 IEEE 9th Int Symp Biomed Imaging 2012:968–71. doi:10.1109/isbi.2012.6235718.
[21] Bredies K, Kunisch K, Pock T. Total Generalized Variation. SIAM J Imaging Sci 2010;3:492–526. doi:10.1137/090769521.
[22] Knoll F, Bredies K, Pock T, Stollberger R. Second Order Total Generalized Variation (TGV) for MRI. Magn Reson Med 2011;65:480–91. doi:10.1002/mrm.22595.
[23] Guo W, Qin J, Yin W. A New Detail-Preserving Regularization Scheme. SIAM J Imaging Sci 2014;7:1309–34. doi:10.1137/120904263.
[24] Chen C, Huang J. Exploiting the wavelet structure in compressed sensing MRI. Magn Reson Imaging 2014.
[25] Hu C, Qu X, Guo D, Bao L, Chen Z. Wavelet-based edge correlation incorporated iterative reconstruction for undersampled MRI. Magn Reson Imaging 2011;29:907–15. doi:10.1016/j.mri.2011.04.016.
[26] Kayvanrad MH, McLeod AJ, Baxter JSH, McKenzie CA, Peters TM. Stationary wavelet transform for under-sampled MRI reconstruction. Magn Reson Imaging 2014;32:1353–64. doi:10.1016/j.mri.2014.08.004.
[27] Ning B, Qu X, Guo D, Hu C, Chen Z. Magnetic resonance image reconstruction using trained geometric directions in 2D redundant wavelets domain and non-convex optimization. Magn Reson Imaging 2013;31:1611–22. doi:10.1016/j.mri.2013.07.010.
[28] Qu X, Guo D, Ning B, Hou Y, Lin Y, Cai S, et al. Undersampled MRI reconstruction with patch-based directional wavelets. Magn Reson Imaging 2012;30:964–77.
[29] Jacques L, Duval L, Chaux C, Peyre G. A panorama on multiscale geometric representations, intertwining spatial, directional and frequency selectivity. Signal Processing 2011;91:2699–730. doi:10.1016/j.sigpro.2011.04.025.
[30] Gho S-M, Nam Y, Zho S-Y, Kim EY, Kim D-H. Three dimension double inversion recovery gray matter imaging using compressed sensing. Magn Reson Imaging 2010;28:1395–402. doi:10.1016/j.mri.2010.06.029.
[31] Qu X, Zhang W, Guo D, Cai C, Cai S, Chen Z. Iterative thresholding compressed sensing MRI based on contourlet transform. Inverse Probl Sci Eng 2010;18:737–58. doi:10.1080/17415977.2010.492509.
[32] Gopi VP, Palanisamy P, Wahid KA, Babyn P. MR image reconstruction based on framelets and nonlocal total variation using split Bregman method. Int J Comput Assist Radiol Surg 2014;9:459–72. doi:10.1007/s11548-013-0938-z.
[33] Pejoski S, Kafedziski V, Gleich D. Compressed Sensing MRI Using Discrete Nonseparable Shearlet Transform and FISTA. IEEE Signal Process Lett 2015;22:1566–70. doi:10.1109/lsp.2015.2414443.

[34] Hong M, Yu Y, Wang H, Liu F, Crozier S. Compressed sensing MRI with singular value decomposition-based sparsity basis. Phys Med Biol 2011;56:6311–25. doi:10.1088/0031-9155/56/19/010.
[35] Cai J-F, Ji H, Shen Z, Ye G-B. Data-driven tight frame construction and image denoising. Appl Comput Harmon Anal 2014;37:89–105. doi:10.1016/j.acha.2013.010.001.
[36] Ravishankar S, Bresler Y. MR Image Reconstruction From Highly Undersampled k-Space Data by Dictionary Learning. IEEE Trans Med Imaging 2011;30:1028–41. doi:10.1109/tmi.2010.2090538.
[37] Huang J, Guo L, Feng Q, Chen W, Feng Y. Sparsity-promoting orthogonal dictionary updating for image reconstruction from highly undersampled magnetic resonance data. Phys Med Biol 2015;60:5359–80. doi:10.1088/0031-9155/60/14/5359.
[38] Buades A, Coll B, Morel JM. A review of image denoising algorithms, with a new one. Multiscale Model Simul 2005;4:490–530. doi:10.1137/040616024.
[39] Dabov K, Foi A, Katkovnik V, Egiazarian K. Image denoising by sparse 3-D transform-domain collaborative filtering. Ieee Trans Image Process 2007;16:2080–95. doi:10.1109/tip.2007.901238.
[40] Bao L, Robini M, Liu W, Zhu Y. Structure-adaptive sparse denoising for diffusion-tensor MRI. Med Image Anal 2013;17:442–57. doi:10.1016/j.media.2013.01.006.
[41] Qu X, Hou Y, Lam F, Guo D, Zhong J, Chen Z. Magnetic resonance image reconstruction from undersampled measurements using a patch-based nonlocal operator. Med Image Anal 2014;18:843–56. doi:10.1016/j.media.2013.09.007.
[42] Daubechies I, Han B, Ron A, Shen ZW. Framelets: MRA-based constructions of wavelet frames. Appl Comput Harmon Anal 2003;14:1–46. doi:10.1016/s1063-5203(02)00511-0.
[43] Cai J-F, Shen Z. Framelet based deconvolution. J Comput Math 2010;28:289–308. doi:10.4208/jcm.1001-m1002.
[44] Ron A, Shen ZW. Affine systems in L-2(R-d): The analysis of the analysis operator. J Funct Anal 1997;148:408–47. doi:10.1006/jfan.1996.3079.
[45] Chan RH, Riemenschneider SD, Shen LX, Shen ZW. Tight frame: an efficient way for high-resolution image reconstruction. Appl Comput Harmon Anal 2004;17:91–115. doi:10.1016/j.acha.2004.02.003.
[46] Huang J, Zhang S, Metaxas D. Efficient MR image reconstruction for compressed MR imaging. Med Image Anal 2011;15:670–9. doi:10.1016/j.media.2011.06.001.
[47] Carrillo RE, McEwen JD, Wiaux Y. Sparsity Averaging Reweighted Analysis (SARA): a novel algorithm for radio-interferometric imaging. Mon Not R Astron Soc 2012;426:1223–34. doi:10.1111/j.1365-2966.2012.21605.x.
[48] Wang Z, Bovik AC, Sheikh HR, Simoncelli EP. Image quality assessment: From error visibility to structural similarity. Ieee Trans Image Process 2004;13:600–12. doi:10.1109/tip.2003.819861.